Preprints.org

Article

Not peer-reviewed version

Connectivity of Mangrove Crab Populations Reveal Potential Exposure of Larvae to Metaloid Pollutants

Nelson Gouveia , Sabrina Fonseca , Lucas Mota * , Manuela Santana , Douglas Francisco Marcolino Gherardi , Maikon Di Domenico , Kyssyane Oliveira , Fábio Cavalca Bom , Nadson Simões , Gisele Daiane Pinha , Renato Ghisolfi , Mônica Maria Pereira Tognella , Fabian Sá , Fabiana Costa , Iurick Saraiva , Fábio Ribeiro , Laís Altoé Porto , Karen Otoni de Oliveira Lima , Beatrice Ferreira

Posted Date: 24 March 2026

doi: 10.20944/preprints202603.1937.v1

Keywords: larval connectivity; marine pollution; ocean modeling; *Ucides cordatus*; Doce river

Preprints.org is a free multidisciplinary platform providing preprint service that is dedicated to making early versions of research outputs permanently available and citable. Preprints posted at Preprints.org appear in Web of Science, Crossref, Google Scholar, Scilit, Europe PMC.

Copyright: This open access article is published under a Creative Commons CC BY 4.0 license, which permit the free download, distribution, and reuse, provided that the author and preprint are cited in any reuse.

Preprints.org (www.preprints.org) | NOT PEER-REVIEWED | Posted: 24 March 2026 doi:10.20944/preprints202603.1937.v1

Disclaimer/Publisher's Note: The statements, opinions, and data contained in all publications are solely those of the individual author(s) and contributor(s) and not of MDPI and/or the editor(s). MDPI and/or the editor(s) disclaim responsibility for any injury to people or property resulting from any ideas, methods, instructions, or products referred to in the content.

Article

Connectivity of Mangrove Crab Populations Reveal Potential Exposure of Larvae to Metaloid Pollutants

Nelson Gouveia [1,2], Sabrina Fonseca [3], Lucas Mota [2,5,*], Manuela Santana [4], Douglas Francisco Marcolino Gherardi [5], Maikon Di Domenico [4], Kyssyane Oliveira [6], Fábio Cavalca Bom [7], Nadson Simões [8], Gisele Daiane Pinha [8], Renato Ghisolfi [3], Mônica Maria Pereira Tognella [9], Fabian Sá [6], Fabiana Costa [8], Iurick Saraiva [2], Fábio Ribeiro [10], Laís Altoé Porto [11], Karen Otoni de Oliveira Lima [11] and Beatrice Ferreira [2]

[1] Department of Geography, University of Victoria, BC, Victoria, Canada
[2] Department Oceanography, Federal University of Pernambuco, UFPE, Recife, Brazil
[3] Laboratory of Physical Oceanography, Federal University of Espirito Santo, UFES, Vitória, Brazil
[4] Center for Marine Studies, Federal University of Paraná, UFPR, Paraná, Brazil
[5] Laboratory of Ocean and Atmosphere Studies (LOA), National Institute for Space Research, INPE, São José dos Campos, Brazil
[6] Federal University of Espirito Santo, UFES, Vitória, Brazil
[7] Laboratory of Environmental Geochemistry and Marine Pollution, (LabGAm), Federal University of Espirito Santo, UFES, Vitória, Brazil
[8] Federal University of Southern Bahia, UFSB, Brazil
[9] Department of Agrarian and Biological Sciences, Federal University of Espirito Santo, UFES, São Mateus, Brazil
[10] National Institute of Science and Technology of Biodiversity of the Blue Amazon, (INCT-BAA), Belém, Brazil
[11] Foundation of Technology Espirito Santo, Federal University of Espirito Santo, UFES, Vitória, Brazil
* Correspondence: lucas.mota@inpe.br

Abstract

Large-scale disasters can result in chronic pollution of coastal environments with unanticipated and poorly quantified impacts, such as the reshaping of marine connectivity. A recent example is the collapse of the Fundão tailings dam in 2015 that released about 50 million m^3 of mine waste into the Doce River, affecting one of Brazil's largest estuarine–mangrove systems. Here, we combine a high-resolution CROCO hydrodynamic simulation with an individual-based Lagrangian model (Ichthyop) to track the dispersal of mangrove crab (*Ucides cordatus*) larvae from four estuaries along the southeastern Brazilian margin between 2022 and 2024. Trajectories crossing toxicity fields derived from in situ collections (msPAF, based on species sensitivity distributions) were used to quantify larval exposure to contaminants from mine waste. Results show that surface shelf flow and mesoscale activity in the vicinity of the Doce river mouth contribute to offshore export of larvae, while the reef-dominated Abrolhos shelf promotes retention. Interannual variability alternates between long-distance export and local retention, likely reflecting climate-driven anomalies such as ENSO. Larval mortality rates caused by offshore advection and lethal temperature are high (65–75%), with surviving cohorts frequently crossing high-contamination zones. This suggests that the regional connectivity of *U. cordatus* is under chronic stress that likely compromises the integrity and resilience of coastal populations, since southern estuaries depend strongly on northern larval sources. The integration of Lagrangian simulations with in-situ contaminant monitoring and spatially explicit exposure metrics demonstrate that transport pathways regulate not only connectivity among estuaries but also the duration and intensity of larval exposure to pollutants.

Keywords: larval connectivity; marine pollution; ocean modeling; *Ucides cordatus*; Doce river

© 2026 by the author(s). Distributed under a Creative Commons CC BY license.

Preprints.org (www.preprints.org) | NOT PEER-REVIEWED | Posted: 24 March 2026 doi:10.20944/preprints202603.1937.v1

1. Introduction

On November 5, 2015, the Fundão tailings dam collapsed in Mariana Municipality (Minas Gerais, Brazil), releasing approximately 50 million m³ of iron ore waste into the Doce River. Within 17 days, the metal-contaminated plume reached the river mouth and dispersed along hundreds of kilometers of estuarine and mangrove habitats of Atlantic Ocean [1–5] As Brazil's worst environmental disaster and one of the largest mining accidents worldwide [6–8], its effects on coastal ecosystems persist, with remobilized sediments transporting metals that alter water quality, benthic habitats, and the resilience of mangrove and estuarine communities [4,5,9–13].

The mud crab *Ucides cordatus* (Linnaeus, 1763) is a fundamental component of Brazilian mangroves, shaping sediment dynamics, nutrient cycling, and supporting local fisheries and livelihoods [14–18]. Its biphasic life cycle includes a planktonic larval phase lasting an average of 20 to 60 days, followed by settlement of the megalopa stage in estuaries [19–23]. *U. cordatus* occurs along the entire Brazilian coastline, including all major mangrove systems in the southeastern region; its continuous latitudinal distribution from Amapá to Santa Catarina [15,24]. This species exhibits high population connectivity across various coastal regions of Brazil, facilitated by larval dispersal via ocean currents [25]. During this dispersive marine phase (mainly zoea stages), larvae are likely to be exposed to contaminants present in the disaster-affected area capable of disrupting physiological development and behavioral regulation. Even when not directly lethal, such exposures may reduce larval fitness, with implications for recruitment success, reproductive potential, and the demographic stability of interconnected populations [26].

Furthermore, the return of the final larval stage (megalopal) to the estuary and recruitment in distant mangroves may carry modified biological characteristics, propagating the effects of contamination through population networks and altering ecosystem dynamics along the coast. Evidence from the Doce River plume shows negative effects on zooplankton, including reduced diversity and increased opportunistic species linked to higher concentrations of Al, Mn, and Fe [27], metals known to impair crustacean larval development and morphology [28,29]. Recent findings reinforce this concern, as *U. cordatus* populations show vulnerability in terms of average size and density, indicating risks to stock maintenance when environmental impacts become chronic and compromise adaptive capacity [12]. In this way, the Fundão disaster may continue to influence mangrove communities beyond the initially affected sites, jeopardizing the livelihoods of numerous traditional communities in the affected mangrove forests that depend on the capture of *U. cordatus*.

Although these physical processes are well characterized, their influence on larval transport, retention, and settlement remains poorly understood, representing a critical gap in linking oceanographic dynamics to biological connectivity along the southeastern Brazilian coast. The Brazil Current (BC), a western boundary current transporting warm tropical waters southward, interacts with complex shelf topography, including the wide Abrolhos Bank and the narrower Espírito Santo shelf. This interaction induces encroachment, generates mesoscale features such as the Abrolhos anticyclone eddy and Vitória cyclone eddy, which drive vertical mixing, nutrient enrichment, and offshore plumes [30–33].

Genetic studies reveal weak differentiation among *U. cordatus* populations, consistent with high connectivity of metapopulations that may be facilitated by these circulation patterns and efficient larval transport [25]. Connectivity is further reinforced during the plankton-to-benthos transition, when megalopae enter estuaries and recruit to new grounds. However, while genetic evidence suggests high connectivity, the potential for contaminants to modify larval traits raises pressing questions: How are mangroves linked through larval dispersal? To what extent might larvae exposure near the Doce River impact populations in other mangroves? Are there additional sites that require monitoring to detect long-term impacts? Understanding these patterns is essential to assessing the persistence and propagation of historical contamination along the coast.

We hypothesize that larvae originating from mangroves near the Doce River may become exposed to contaminants and physical stressors during their planktonic phase, an exposure that may potentially alter mortality rates during their life stage in the marine environment, influencing

© 2026 by the author(s). Distributed under a Creative Commons CC BY license.

Preprints.org (www.preprints.org) | NOT PEER-REVIEWED | Posted: 24 March 2026 doi:10.20944/preprints202603.1937.v1

population connectivity and demographic dynamics along the Brazilian coast. To test this hypothesis, we aimed to (i) analyze the spatial reach of potentially affected larvae, (ii) quantify exposure duration to assess the likelihood of sublethal effects, and (iii) evaluate larval connectivity potential between mangrove spawning sites to understand how local contamination could propagate through regional metapopulations. These analyses provide a mechanistic framework to examine how historical pollution may continue to shape the distribution, recruitment, and resilience of *U. cordatus* populations and the mangrove ecosystems they inhabit.

2. Materials and Methods

2.1. Larval Dispersion Modelling

Larval dispersal experiments were conducted along the Brazilian coast, encompassing the Abrolhos Bank and the Vitória–Trindade Ridge (Figure 1). Four mangrove systems monitored [5] were selected as spawning sites for larval release: (A) Caravelas; (B) São Mateus; (C) Doce River; and (D) Piraquê-Açu-Mirim, spanning from southern Bahia to the mouth of the Doce River (Figure 1). These sites were chosen because they represent major mangrove systems and they are adjacent to the Doce River plume, where adult populations of *U. cordatus* are established and reproductive activity is well documented. Potential recruitment areas were defined based on the presence of mangrove habitats along the coast (details in section 2.1.2), including not only the four spawning sites (A–D), where local retention may occur, but also additional mangrove systems to the south: (E) São João da Barra; (F) Cabo Frio; and (G) Rio de Janeiro, between southern Espirito Santo and Rio de Janeiro. All these areas provide suitable habitat for larval settlement and post-larval development.

Surface circulation in the region is dominated by the Brazil Current (BC), a western boundary current formed at the bifurcation of the South Equatorial Current around 14°S [30,31]. The BC flows southward along the continental shelf break, transporting tropical waters in the upper ~0 – 150 m of the water column. In this sector, it is confined to the upper ~150–250 m, with a core width of about 100 – 200 km and surface velocities typically ranging from 0.5 to 1.0 m s^{-1} [32,34]. During the austral winter (June–August), the intensity of the BC decreases and its axis shifts slightly southward, altering regional water transport. The interaction of the BC with the shelf break also generates quasi-stationary mesoscale vortices between 14°S and 20°S [32]. This circulation regime is characterized by the Abrolhos anticyclone (AE, ~19°S) and the Vitória cyclone (VE, ~22°S), which form a dipolar structure that promotes the uplift of cold, nutrient-rich waters, subsequently mixed in the upper layer and advected offshore as a plume extending more than 250 km from the shelf break [33].

The formation and persistence of these mesoscale features are strongly modulated by the morphology of the continental shelf. The Abrolhos Bank, located between ~16°S and 19°S, is the broadest shelf sector in the South Atlantic, extending up to ~200 km offshore and covering ~45,000 km^2 [35]. Its bathymetry is characterized by a wide, gently sloping platform with extensive reef structures and carbonate banks, contrasting sharply with the narrow shelf of Espírito Santo, which is only ~50 – 80 km wide and bounded by a steep slope. This abrupt latitudinal change in shelf geometry enhances vorticity and favors the generation, trapping, and maintenance of mesoscale eddies, providing the physical setting for the AE – VE dipole [34,35]. Over the Abrolhos Bank, circulation is further influenced by reef-induced topographic steering and localized retention, whereas in the Espírito Santo sector, shelf–slope interactions facilitate intrusions of slope waters onto the shelf. These bathymetric and geomorphological contrasts modulate vertical mixing, nutrient enrichment through episodic upwelling, and the variability of surface transport in the region.

© 2026 by the author(s). Distributed under a Creative Commons CC BY license.

Preprints.org (www.preprints.org) | NOT PEER-REVIEWED | Posted: 24 March 2026 doi:10.20944/preprints202603.1937.v1

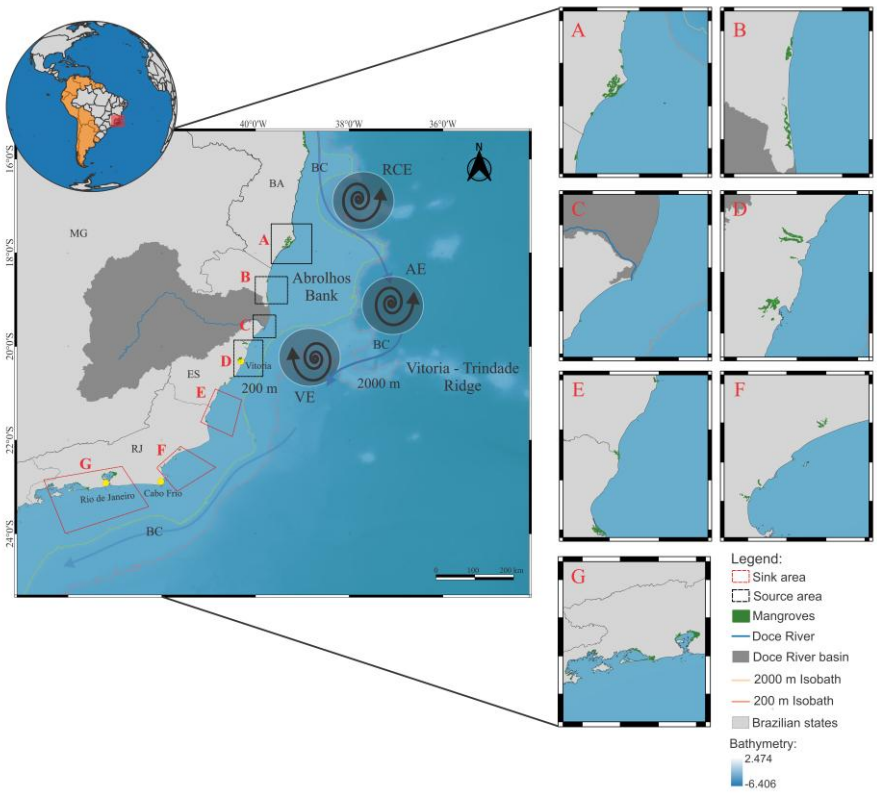

Figure 1. Study area showing the spawning (larval release) sites Caravelas (A), São Mateus (B), Doce River (C), and Piraquê-Açu-Mirim (D) (black polygons). Potential recruitment areas, defined based on the presence of suitable mangrove habitat, include São João da Barra (E), Cabo Frio (F), and Rio de Janeiro (G) (red polygons), as well as the spawning sites, where local retention may occur. Mangrove areas are shown in green. A schematic representation of the Brazil Current (BC), the Royal Charlotte Eddy (RCE), the Abrolhos Eddy (AE), and the Vitória Eddy (VE) is shown. The 200 m isobath, marking the continental shelf break, is depicted in yellow, and the 2000 m isobath in pink.

2.1.1. Hydrodynamic Model

The Coastal and Regional Ocean Community model (CROCO, version 1.2), an oceanic modeling system built upon ROMS_AGRIF, was employed to simulate the ocean circulation of the study region between 2022 and 2024. CROCO is a three-dimensional, free-surface, terrain-following model that solves the Reynolds-averaged Navier-Stokes equations using hydrostatic and Boussinesq approximations as in ROMS [36–39].

A regular horizontal grid was implemented for the study area (49°W-27°W and 27°S-8°S) with approximately 4.6 km spatial resolution. The grid features open eastern, southern, and northern boundaries, with a closed western boundary. The vertical coordinate consists of 40 sigma levels, irregularly spaced and higher resolution near the surface. The bathymetric data were obtained from the General Bathymetric Chart of the Oceans (GEBCO)[40]with a spatial resolution of 30 arc-seconds. Surface forcing conditions were obtained from ERA5 reanalysis produced by European Center for Medium-Range Weather Forecasts with temporal resolution of 1 hour and spatial resolution of 31 km [41].

Tidal forcing was obtained from the TPXO 9.0 global database [42] (Egbert and Erofeeva, 2002), which provided amplitudes and phases of the major tidal harmonic constituents at spatial resolution of 1/4ox1/4o applied at the open boundaries (M2, S2, N2, K2, K2, O1, P1, Q1, Mf and Mm). The HYbrid Coordinate Ocean Model (HYCOM Global 1/12o, approximately 9.25 km of horizontal resolution) coupled with the Navy Coupled Ocean Data Assimilation (NCODA) system reanalysis (HYCOM) provided the initial and daily boundary conditions, including temperature, salinity, sea surface

© 2026 by the author(s). Distributed under a Creative Commons CC BY license.

Preprints.org (www.preprints.org) | NOT PEER-REVIEWED | Posted: 24 March 2026 doi:10.20944/preprints202603.1937.v1

elevation, and current velocities [43]. The simulations closely matched the observed data and accurately represented the circulation processes of the region, demonstrating the robustness of the model.

2.1.2. Lagrangian Model

The larval dispersal experiments for U. cordatus were conducted using the Lagrangian dispersal model (individual-based model, IBM) Ichthyop v3.3 [44]. This is a Java-based open-source tool designed to study particle dispersion by integrating physical and biological factors that influence larval dynamics throughout the water column. Ichthyop uses vector fields of current velocity, temperature, and salinity from hydrodynamic models to simulate advection and connection paths of virtual particles in a three-dimensional physical environment. In this study, reproductive aspects of *U. cordatus* obtained from the literature (Table 1) were used. Spawning of the species always occurs after the full and new moon during the months of January to April in the study region [45,46]. Twelve simulations were conducted from 2022 to 2024, four for each year, four for the entire period, each lasting 30 days with a time step of 2 hours.

Table 1. Biological parameters of U. cordatus used as input for biological simulation experiments.

Parameters	*U. cordatus*	References
Total number of released particles	96.000	-
Pelagic larval duration	30 days	[45]
Spawning season	January to April	[45,46]
Lunar phases	After full and new moon	[45]
Diel vertical migration depth	-20 (day) to -30 (night) m	[47]
Temperature optimum range	(20°C to 30°C)	[19,48]
Turbulent dissipation rate	$1x10^{-9}$ m².s−3	[49]
Sunset and sunrise	6:00 e 18:00	-
Coastline behaviour	Bouncing	-
Advection method	Runge Kutta 4	-
Simulation years	2022 to 2024	-

The survival and mortality rates of the larvae were calculated after the end of the simulations, in which mortalities were divided into lethal temperature (outside the survival range) and advection (outside the model domain) calculated according to Equation (1).

$$Mortality_t = \frac{\sum_t di}{\sum_t C} \quad (1)$$

where: t is the time instant for each simulation; di are the larvae advected to regions outside the temperature range and/or outside the domain; c is the total number of particles spawned.

2.2. Larval Exposure Assessment

Larval exposure to potentially contaminated waters was quantified by integrating simulated trajectories with in situ environmental data and Doce River sediment plume distributions. An exposure index was calculated for each larva, reflecting both duration and intensity of contact with contaminated waters. This approach allowed a spatially and temporally explicit assessment of the potential impacts of historical contamination on dispersing larvae.

© 2026 by the author(s). Distributed under a Creative Commons CC BY license.

Preprints.org (www.preprints.org) | NOT PEER-REVIEWED | Posted: 24 March 2026 doi:10.20944/preprints202603.1937.v1

2.2.1. In situ Data and NOEC index

To quantify the potential toxic pressure of metal(loid)s on *U. cordatus* larvae, we used water quality data collected during campaigns from 2022 to 2024 (Figure S1). Water samples were obtained at both surface (0–15 cm) and near-bottom (~50 cm above sediment) layers using non-metallic, messenger-activated bottles. Samples were carefully transferred to pre-cleaned containers with silicone tubing, and all handling was performed with powder-free nitrile gloves to minimize contamination. Total, dissolved, and particulate metal(loid)s were analyzed. The dissolved fraction was defined as the material passing through 0.45 µm membranes, whereas the retained fraction constituted the metal(loid)s associated with suspended particulate matter (SPM). Environmental quality assessment in a marine coastal area impacted by mining tailing using a geochemical multi-index and physical approach, provides the analytical framework and indices applied to characterize contamination patterns in this region; for further analytical details, see [50].

For metal(loid)s measured (As, Ba, Cd, Co, Cr, Cu, Fe, Hg, Mn, Ni, Pb, V, Zn, and Al), species sensitivity distributions (SSDs) were constructed using NOEC (No Observed Effect Concentration) and EC10 data [51], which describe the range of sensitivities among species. For each metal(loid), a hazard unit (HU) was calculated as the ratio between the measured environmental concentration and the SSD mean, representing the relative toxic pressure of that metal(loid). The hazard units of all metal(loid)s were combined to calculate the multi-substance Potentially Affected Fraction (msPAF), which estimates the fraction of species potentially affected by the mixture. msPAF values ≤ 0.05 indicate protection of at least 95% of species, and the contribution of each metal(loid) to the cumulative msPAF was expressed as a proportion of total hazard units to identify the most influential contaminants. Raster layers representing NOEC-based thresholds were created for each campaign and season (dry and rainy), summarizing the spatial distribution of potentially toxic concentrations.

2.2.2. Larval Exposure Metric

Larval exposure to metal contamination was quantified by coupling simulated larval trajectories with spatially and temporally resolved msPAF fields. msPAF values derived from in situ measurements were first interpolated onto regular raster grids covering the entire study domain. Separate raster layers were generated for each monitoring campaign and aggregated by season, defining rainy (October–March) and dry (April–September) periods to capture seasonal variability in contaminant distribution [52].

Larval positions were tracked at 6-hour intervals over the 30-day pelagic larval duration using outputs from the Lagrangian simulations. At each time step, larval locations were overlaid onto the corresponding seasonal msPAF raster, and the msPAF value of the occupied grid cell was assigned to each larva. Exposure was recorded whenever a larva occupied a cell with msPAF values greater than 0.05, a threshold indicative of potential toxic effects on at least 5% of species.

Cumulative exposure time for each larva was calculated as the total number of time steps spent in grid cells exceeding the msPAF threshold, multiplied by the temporal resolution (6 hours). This metric integrates both the duration and spatial persistence of exposure during larval transport. Exposure times were calculated independently for each spawning site, simulation month, and year between 2022 and 2024.

2.3. Connectivity Among Mangroves Populations

The connectivity analyses considered a total of seven different areas from which only four were used as spawning areas (A to D in Figure 1) under the direct influence of the Doce River plume [5] (Tognella et al., 2022). Recruitment was computed for all seven areas (A to G in Figure 1) to assess the potential pollution impacts on populations to the south of the Doce River mouth influenced by the transport of the BC. Maps depicting the final positions of living larvae provide an estimate of spatial aggregation and allow the identification of regions with a higher probability of colonization. Each area was defined using a buffer around the mangroves extracted from Global Mangrove Watch

© 2026 by the author(s). Distributed under a Creative Commons CC BY license.

Preprints.org (www.preprints.org) | NOT PEER-REVIEWED | Posted: 24 March 2026 doi:10.20944/preprints202603.1937.v1

(GMW), an online platform that provides remote sensing data and the tools needed to monitor mangroves with global access to near real-time information (https://www.globalmangrovewatch.org/). The mangrove product demonstrates the global extent of mangrove forests for the year 2020, derived from Random Forest classification of a combination of L-band radar data (ALOS PALSAR) and optical satellite data (Landsat-5 and Landsat-7) [55] (black and red polygons in Figure 1), representing the spatial extent of suitable settlement habitat. This buffer approach accounts for small-scale spatial uncertainty in larval positions and habitat boundaries, ensuring that local retention and recruitment events are captured even if larvae do not land precisely on mapped mangrove polygons. Successful recruitment and local retention are considered if a larva reaches the buffer area at the end of the 30-days simulation. This procedure was applied to each individual simulation to account for intra-seasonal variability in larval dispersal, and four simulations were conducted for the spawning period.

Connectivity between areas was then quantified and presented as connectivity maps, summarizing the proportion of surviving larvae moving from origin to destination areas. This approach allows the identification of regions with higher potential for larval settlement and explicitly accounts for the effects of environmental drivers on connectivity patterns, addressing spatial heterogeneity and larval retention dynamics that could influence recruitment outcomes. The percentages were calculated using the following Equation (2 and 3).

$$Recruitment_{t,i} = \frac{\sum_t Cij + \sum_t Cii}{\sum_t Nt} \quad (2)$$

$$Local\ retention_{t,i} = \frac{\sum_t Cii}{\sum_t Ni} \quad (3)$$

where: t is the time instant for each simulation; Cij represents the larvae generated in region i that were recruited in region j; Cii is the number of larvae generated in region i that were recruited in the same region. Nt is the total number of larvae generated in the simulation and Ni is the number of particles generated in region i.

3. Results

3.1. Variability of Dispersion Trajectories and Distances Traveled by Larvae

The dispersion of living *U. cordatus* larvae released from Caravelas, São Mateus, Doce River, and Piraquê-Açu-Mirim exhibits a consistent southward orientation throughout the analysed period (January–April of 2022, 2023, and 2024), with trajectories predominantly aligned with the continental shelf and slope (Figure 2a). This large-scale pattern is consistent with the mean circulation resolved by the three-dimensional ocean reanalysis used to force the dispersal simulations, in which the Brazil Current drives meridional transport along the eastern Brazilian margin during the spawning season.

Regional departures from this shelf-aligned transport occur at the northernmost release area, Caravelas (A in Figure 1), where circulation is strongly influenced by the Abrolhos Bank. In this sector, the wide shelf and reef-dominated topography modify flow pathways, resulting in shorter and more curved trajectories compared to those originating from São Mateus, Doce River, and Piraquê-Açu-Mirim (Figure 2a). Consistent with this southward transport, wind climatology indicates a predominance of N and NE winds during the analysed months, accounting for more than 49% of occurrences across the source regions (Figure S2; Table S2). Such winds are known to influence surface circulation over the inner shelf and coastal zone, where wind-driven processes can locally reinforce the mean along-shelf flow.

© 2026 by the author(s). Distributed under a Creative Commons CC BY license.

Preprints.org (www.preprints.org) | NOT PEER-REVIEWED | Posted: 24 March 2026 doi:10.20944/preprints202603.1937.v1

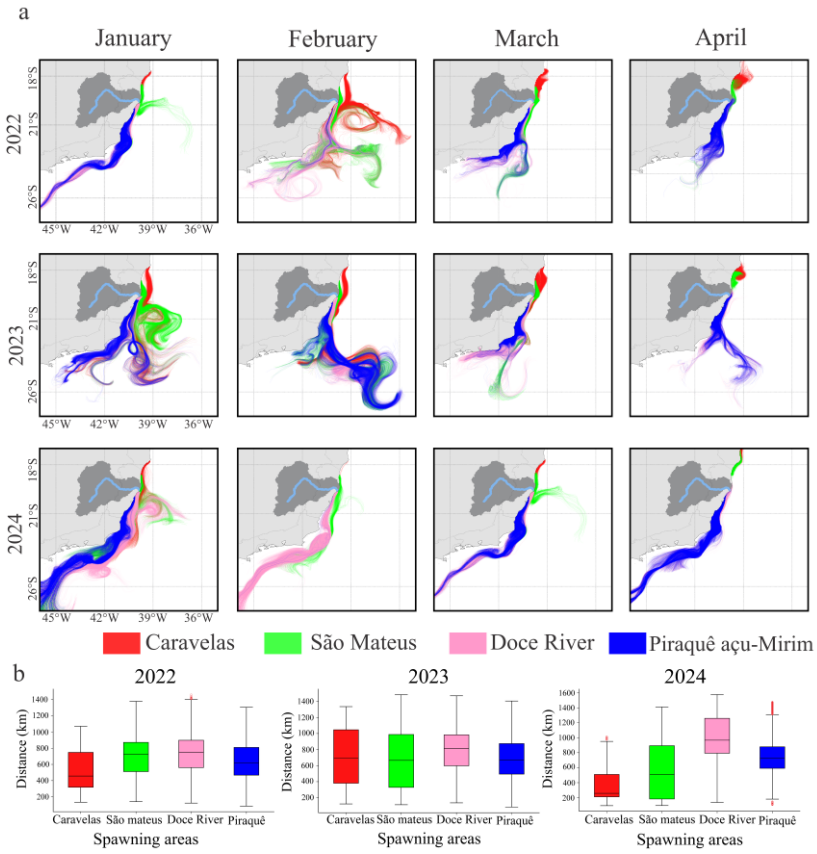

Figure 2. Larval dispersion patterns of the crab *U. cordatus* (a) for the months of January, February, March, and April for the years 2022, 2023, and 2024 superimposed on the Aquatic Biodiversity Monitoring Program (PMBA/Fest) sampling grid (light orange). The colors red, green, pink, and blue represent spawning areas for Caravelas, São Mateus, Doce River, and Piraquê Açu-Mirim, respectively. Boxplots of the total distance traveled by surviving larvae (b) for the spawning years 2022, 2023, and 2024 were calculated separately for each spawning area. The colors of the boxes in red, green, pink, and blue represent the spawning areas of Caravelas, São Mateus, Rio Doce, and Piraquê Açu-Mirim, respectively. The horizontal black lines are the median values, and the outliers are the red circles.

A smaller fraction of particles was occasionally advected eastward, associated with the development of recirculation cells and meanders at the shelf edge, which diverted part of the transport offshore. In April, dispersal patterns diverged among regions. In the Doce River and Piraquê Açu-Mirim, larvae continued to be exported mainly southward, sustained by the large-scale coastal flow and the absence of significant topographic barriers. In São Mateus, however, a marked shift was observed; part of the trajectories moved northward and eastward, linked to the seasonal variability of autumn winds and the intensification of shelf circulation cells, which generated transport opposed to the Brazil Current. This shift coincides with the increase of S and SE winds in April (Figure S2), creating conditions favorable to northward transport and explaining the late-season deviation observed in the simulations. In contrast, Caravelas maintained localized dispersal, with short and recirculating trajectories. The particular configuration of the Abrolhos Bank, composed of reefs and channels, favours the formation of retention cells that limit the coupling of particles to the boundary flow, resulting in larval confinement even in April. The retention in Caravelas is also compatible with the higher proportion of E and SE winds in several months (often 14–34%), which tend to align transport along the coast and reduce offshore displacement, further reinforcing the localized trajectories produced in this region (Tables S3, S4, and S5).

The larval dispersal distances of *U. cordatus* varied consistently between spawning regions and years (Figure 2b). In 2022, Caravelas had the shortest dispersal distances, with medians close to 400

© 2026 by the author(s). Distributed under a Creative Commons CC BY license.

Preprints.org (www.preprints.org) | NOT PEER-REVIEWED | Posted: 24 March 2026 doi:10.20944/preprints202603.1937.v1

km, while São Mateus and Piraquê had intermediate values, close to 600 km. Meanwhile, larvae spawned in the Doce River had the longest dispersal distances, with medians around 700 km and events exceeding 1,200 km. In 2023, there was a general increase in distances in all regions, with medians between 700 and 900 km, including maximum displacements above 1,300 km. In 2024, the patterns became more heterogeneous: Caravelas showed a significant reduction, with medians close to 300 km, São Mateus values above 800 km, Piraquê intermediate values close to 600 km, and the Doce River had the largest displacements, with medians close to 1,000 km and maximums above 1,400 km.

3.1.1. Survival Rates and Sources of Larval Mortality

Larval survival exhibited marked spatial and interannual variability across the four spawning regions (Figure 3). Larval survival averaged ~30%, influenced by strong environmental pressures. These pressures were dominated by environmental variability, particularly exposure to temperatures approaching lethal thresholds, and by circulation patterns that transport larvae into areas less suitable for successful recruitment. Among all years, 2024 showed the most pronounced declines in the larval survival rate. Caravelas recorded a survival rate of 9.47% and Doce River 16.8%, the lowest values in the time series. Interestingly, Caravelas showed the highest survival rates in 2022 and 2023 (above 50%) with advection the only cause of mortality, whereas in 2024, the lethal temperature became the predominant factor. At the same time, while Doce River presented moderate survival rates in the previous years, in 2024 there was a nearly total dominance of advection resulting in the lowest rates.

On the other hand, São Mateus showed the highest survival rate in 2024 (above 50%), with mortality balanced between advection and temperature, whereas in the previous years, advection was the predominant factor in mortality, with moderate survival rates. Finally, Piraquê-Açu-Mirim displayed intermediate and the most consistent survival rates (~35-40%) across the three years with a slight predominance of advection over lethal temperature.

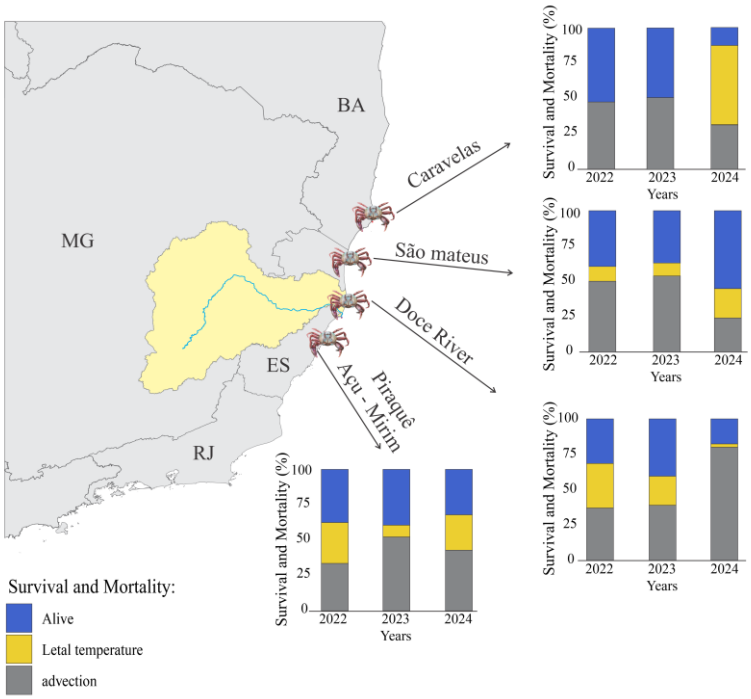

Figure 3. Proportion of particles released from the spawning areas that were alive (blue) or died by lethal temperature (yellow) or were advected to habitats not suitable for recruitment (grey) of *U. cordatus* larvae for the years 2022, 2023, and 2024 for each spawning area (source).

© 2026 by the author(s). Distributed under a Creative Commons CC BY license.

Preprints.org (www.preprints.org) | NOT PEER-REVIEWED | Posted: 24 March 2026 doi:10.20944/preprints202603.1937.v1

Interannual variability in the vertical thermal structure of the water column emerged during the spawning season from temperature records obtained at fixed moorings (Figure 4). Vertical temperature differences (ΔT = Tsurface – Tsubsurface) were computed from temperatures measured near the surface and at a subsurface depth instrumented by the moorings. These moorings are deployed within approximately the same water-column range used by larvae during diel vertical migration (~15–40 m), allowing ΔT to represent vertical thermal gradients within the upper water column. In 2022, ΔT frequently exceeded 4–7 °C between February and April at the Doce River and Piraquê Açu-Mirim sites, indicating persistent stratification during peak spawning months. Over the same period, São Mateus and Caravelas exhibited weak or negligible vertical gradients. The 2023 spawning season showed a comparable spatial pattern, with recurrent ΔT maxima at Doce River and Piraquê Açu-Mirim and lower values at the northern sites. During intervals of elevated ΔT, simulations indicated higher proportions of temperature-driven larval mortality, particularly toward the end of the spawning season (Figure 3).

In 2024, ΔT values remained consistently lower across regions, especially in April, reflecting reduced vertical stratification relative to previous years. Under these conditions, simulations showed lower temperature-driven mortality and increased larval losses associated with advection, consistent with enhanced offshore transport and reduced retention (Figure 3). Wind-stress curl further characterized the physical environment during the spawning period (Figure 4). In 2022 and 2023, extended intervals of negative curl (< 0) occurred from January through March, indicating surface divergence and offshore Ekman transport [54–56]. These intervals overlapped with periods of elevated ΔT. In contrast, curl values in 2024 remained near zero for most of the spawning season, coinciding with weaker vertical gradients and increased vertical mixing, likely associated with seasonal changes in net ocean heat flux [57].

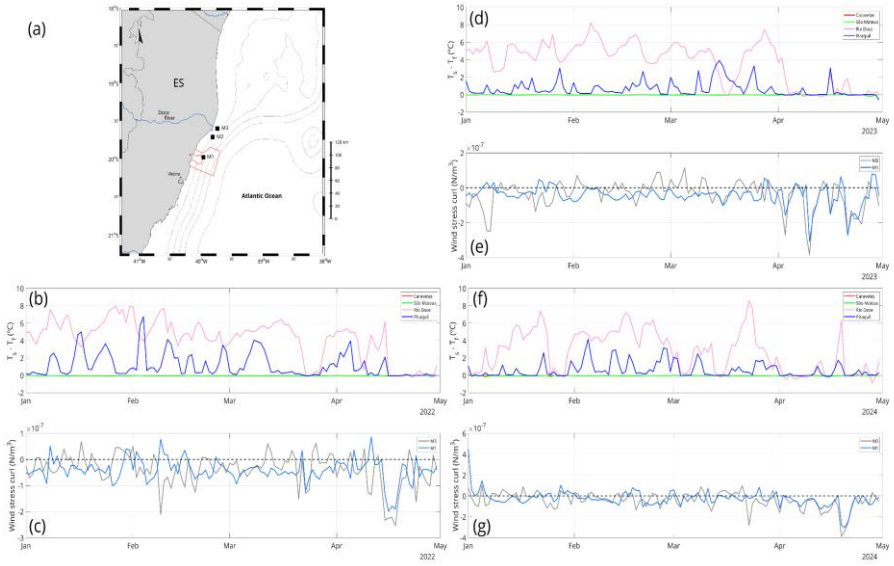

Figure 4. Seasonal evolution of thermal structure and wind-stress curl across spawning years. Panels show daily surface–bottom temperature differences (ΔT = Ts – Tb) for each spawning region (b), (d) and (f) (left) and wind-stress curl at sampling stations F1 and F3 (c), (e) and (g) from January to May during the years 2022, 2023, and 2024.

3.2. Potential Exposure of Larvae to Toxic Metaloids

The analysis of larval exposure in the PMBA monitoring area shows that toxic pressure was present throughout the years studied (Figure 5a). In 2022, the highest toxicity occurred in freshwater zones, at the river mouth, and in the northern sector during the rainy season. This was mainly linked to the metals iron (Fe), copper (Cu), and zinc (Zn). In other areas, toxicity levels were lower (0.05 <

© 2026 by the author(s). Distributed under a Creative Commons CC BY license.

Preprints.org (www.preprints.org) | NOT PEER-REVIEWED | Posted: 24 March 2026 doi:10.20944/preprints202603.1937.v1

msPAF < 0.2), and this general pattern continued during the dry season. In 2023, toxic pressure increased in the northern sector during the rainy season, again driven by the same metals, while freshwater zones remained highly affected. In the dry season, toxicity in freshwater areas decreased, but pressure increased farther offshore on the continental shelf. In 2024, toxic pressure rose again across the entire monitored region, especially in the rainy season, now associated with zinc (Zn), iron (Fe), aluminum (Al), and copper (Cu). During the dry season, pressure decreased in some freshwater zones, particularly in the Lakes sector, as well as in the northern area.

The daily exposure of *U. cordatus* larvae also varied by spawning site (Figure 5b). Larvae spawned in Caravelas were exposed to toxic areas for 6–12 days, especially in March. In São Mateus, exposure lasted 6–15 days, particularly in March and April. By contrast, larvae from the Doce River and Piraquê rivers usually stayed for shorter periods (2–6 days), although some remained 8–12 days, and a few outliers showed exposures longer than 20 days.

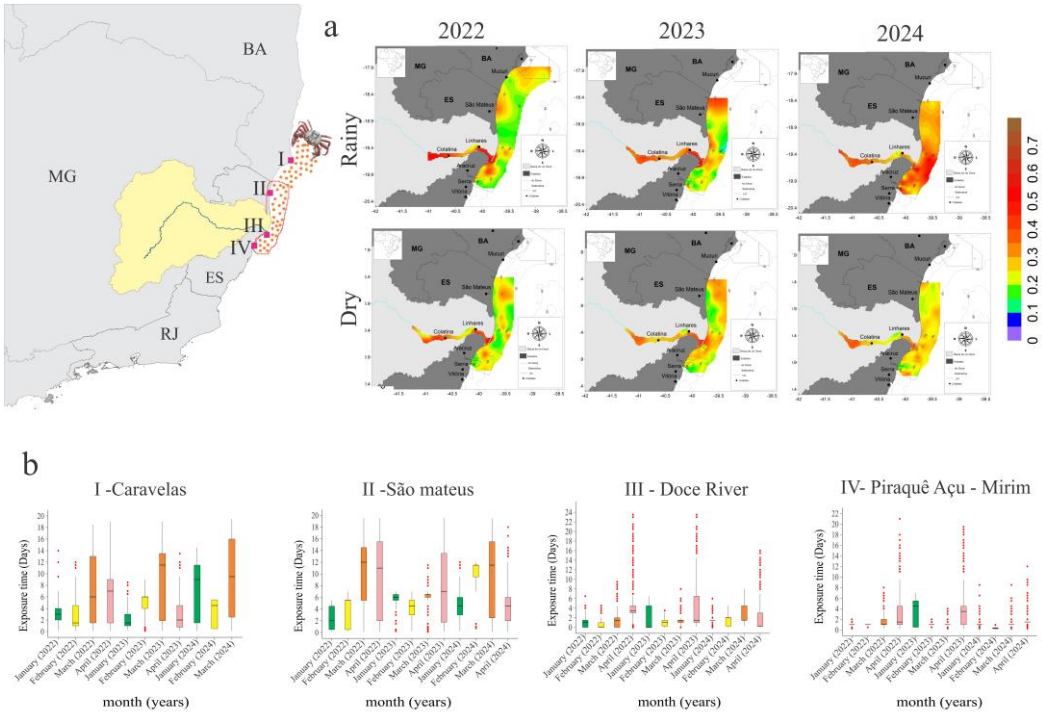

Figure 5. Distribution of msPAF NOEC throughout the monitoring sites between 2022, 2023, and 2024, considering the seasonal variability of the index (i.e., variability between rainy and dry periods). Warmer colors represent a higher probability that freshwater and marine environments are not sufficiently protected, that is, they are vulnerable to the mixture of metals quantified in the water column. (a) Exposure time (boxplots) of *U. cordatus* larvae to the potentially toxic environment monitored by PMBA/Fest (b) during the spawning months and the simulation years 2022, 2023, and 2024 for the spawning areas.

3.3. Spatial and Temporal Variability of Larvae Destination

Final positions of surviving larvae of *U. cordatus* released from the four spawning estuaries during January, February, March, and April between 2022 and 2024 are shown in Figure 6. In January, when spawning began, the larvae released from Caravelas and São Mateus were transported mainly southward along the continental shelf, reaching the coasts of Espírito Santo and northern Rio de Janeiro. Particles released from the Doce River and Piraquê-Açu-Mirim rivers also dispersed southward, concentrating over the middle shelf of Espírito Santo and adjacent offshore areas, with no evidence of return to their release zones. In February, a similar pattern persisted, with most particles distributed along the mid-shelf between northern Espírito Santo and Vitória. Larvae from Caravelas continued to drift southward, though part remained over the Abrolhos Bank. Those from

© 2026 by the author(s). Distributed under a Creative Commons CC BY license.

Preprints.org (www.preprints.org) | NOT PEER-REVIEWED | Posted: 24 March 2026 doi:10.20944/preprints202603.1937.v1

São Mateus and the Doce River exhibited broader dispersion across the outer shelf and slope. In March, final positions indicated reduced dispersal distances and enhanced coastal retention in the Caravelas and São Mateus regions, with particle clusters remaining near the release areas and over the northern sector of the Abrolhos Bank. Larvae from the Doce River and Piraquê-Açu-Mirim remained concentrated farther south, over the Espírito Santo shelf, with limited offshore spread. In April, most particles from Caravelas and São Mateus stayed confined to the inner shelf, indicating predominant local retention during the late spawning period. Larvae from the Doce River and Piraquê-Açu-Mirim remained distributed along the Espírito Santo coast, with part reaching the northern Rio de Janeiro shelf, again without return to source areas.

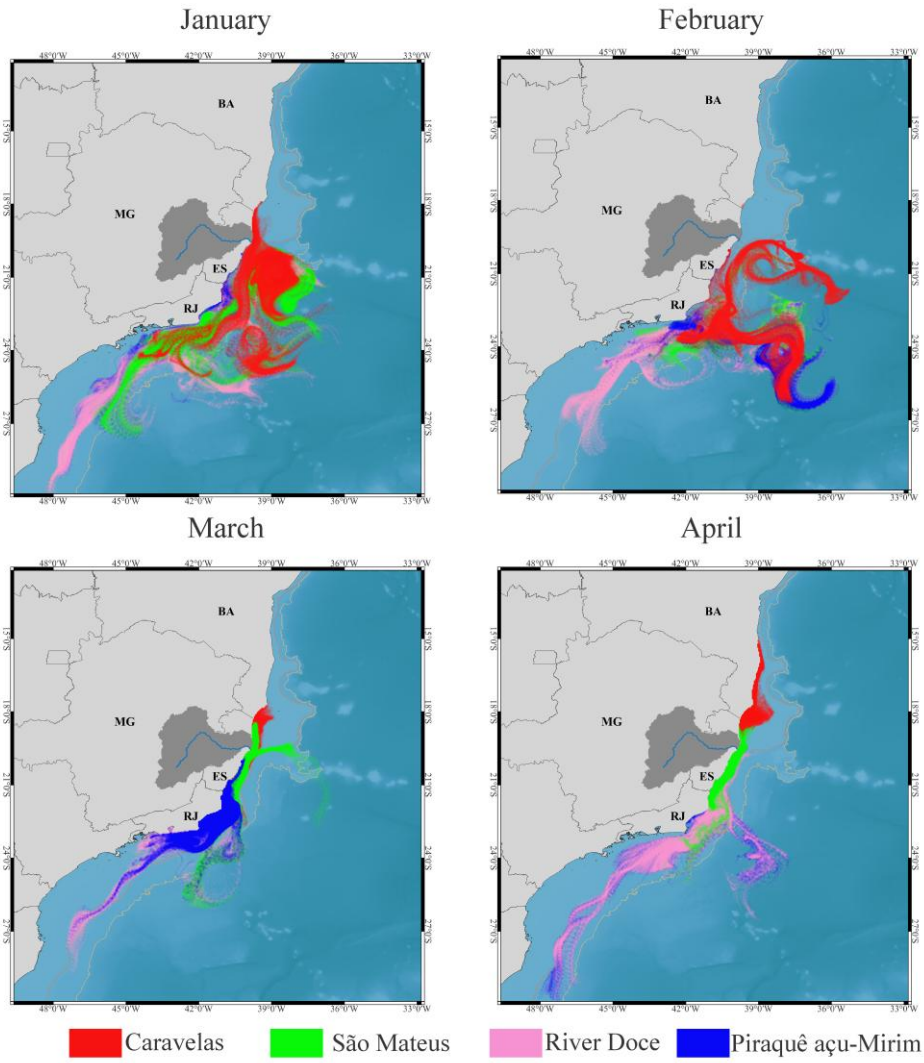

Figure 6. Spatial and temporal destination of U. cordatus larvae released from the four spawning estuaries (Caravelas, São Mateus, Doce River, and Piraquê Açu-Mirim) during January–April, for the 2022–2024 simulations. Colors indicate source regions.

The spatial pattern of the final positions of surviving particles (Figure 6) reflects the large-scale organization of circulation along the southeastern Brazilian shelf. Larvae released from Doce River and Piraquê Açu-Mirim tended to disperse along a well-defined downstream corridor, with endpoints distributed primarily between 19.5°S and 21°S. In contrast, particles originating from Caravelas remained mostly confined to the inner shelf, forming short and localized clusters concentrated north of 18.5°S. São Mateus presented an intermediate behavior, with some trajectories extending southward and others turning offshore depending on the month.

© 2026 by the author(s). Distributed under a Creative Commons CC BY license.

Preprints.org (www.preprints.org) | NOT PEER-REVIEWED | Posted: 24 March 2026 doi:10.20944/preprints202603.1937.v1

3.3.1. Connectivity of Mangroves Recruitment Habitats

Caravelas stands out as a key larval source for the mangroves of São Mateus, São João da Barra, and Piraquê, to which it contributes with approximately 60% of its surviving larvae (Figure 7). Caravelas also displayed significant local retention, as in 2024, when 33% of larvae recruited back into its own mangroves. Although in smaller proportions, larvae spawned in Caravelas occasionally recruited as far as to the Doce River and Rio de Janeiro. Still, São Mateus remained the main destination, receiving on average about 60% of Caravelas originated larvae over the three years analyzed. São Mateus itself showed high local retention, with an average of 48% of surviving larvae recruiting locally. It also acted as a source for the Piraquê and Rio de Janeiro mangroves.

In specific years, such as 2022, 16.5% of larvae recruited to the Doce River, while in 2024, 5% returned to Caravelas, reflecting variable connectivity over time. Larvae spawned in the Doce River also reached potential recruiting grounds in Piraquê and Rio de Janeiro mangroves Rio de Janeiro and Piraquê mangroves. However, unlike other regions, Doce River showed no significant local retention, suggesting that larvae from this area tend to disperse outward. Spawning in Piraquê, on the other hand, contributed mainly to the Rio de Janeiro mangroves, while also showing notable local retention rates, averaging 8% across the study years.

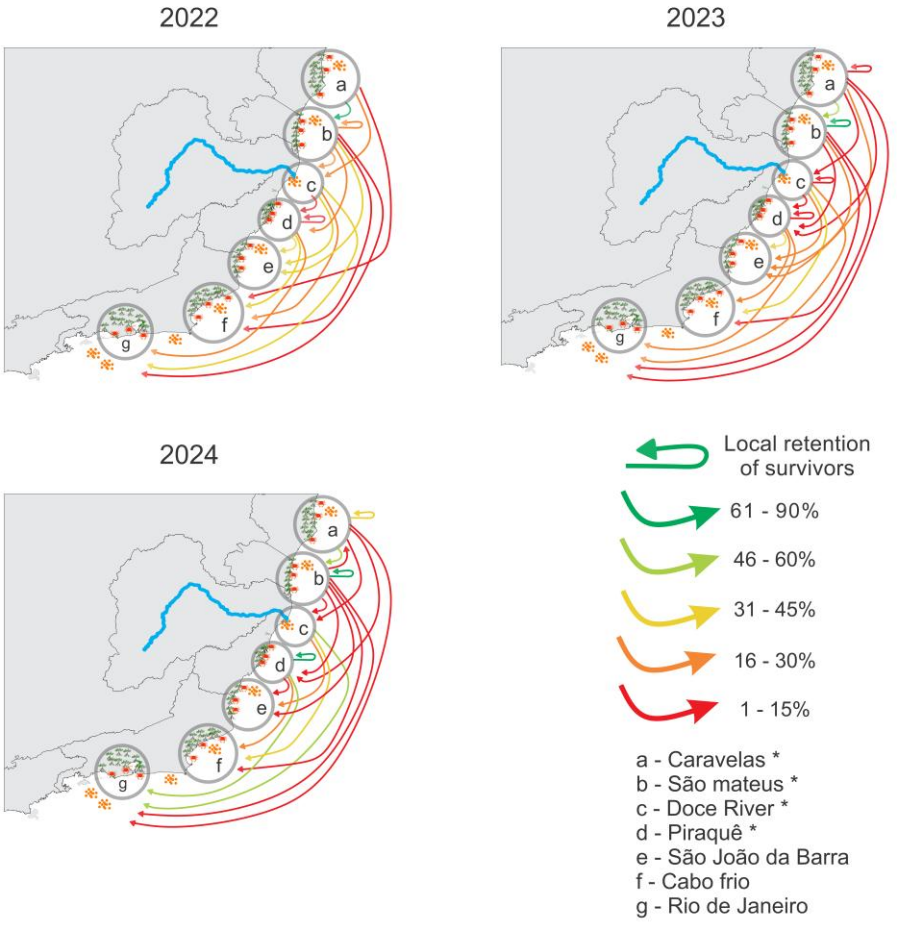

Figure 7. Connectivity rates between mangroves from Caravelas to the state of Rio de Janeiro for the years 2022, 2023, and 2024. The colors of the arrows are related to the percentage of larvae arriving in a region (arrow) from one of the four source regions (start of the arrow highlighted in the legend).

4. Discussion

The present work sheds light on the connectivity of the mud crab *U. cordatus* populations living in coastal mangrove habitats and how it determines the exposure to mining waste contaminants originated from the Mariana tailings dam collapse. Our study reveals that, as expected, larvae of *U.*

© 2026 by the author(s). Distributed under a Creative Commons CC BY license.

Preprints.org (www.preprints.org) | NOT PEER-REVIEWED | Posted: 24 March 2026 doi:10.20944/preprints202603.1937.v1

cordatus are more likely to become exposed to metals associated with the Mariana dam collapse near the Doce River mouth and the coastal zone to the north, where exposure times are higher. Larvae from spawning areas to the south of the river mouth (Doce River and Piraquê Açu-Mirim, C and D in Figure 8) can be exported in relatively large numbers to southernmost regions (up to 60%, as in 2024 shown in Figure 8). This happens as a result of the combined influence of regional circulation and seasonal upwelling acting on the dispersal and survival of larvae. These processes interact to eventually increase larval exposure to persistent contamination associated with the Doce River plume by transporting or retaining these larvae in specific areas. This portion of the western South Atlantic represents a hydrodynamically complex zone of the Brazil Current (BC), where the western boundary flow interacts with contrasting shelf morphologies, the broad and shallow Abrolhos Bank and the narrow, steep Espírito Santo margin [30,32,34]. Within this region, larval transport is controlled by the spatial variability of advection, retention, and cross-shelf exchange governed by tides, mesoscale circulation and wind-driven processes.

The results indicate a consistent seasonal structure in dispersal and connectivity determined by the hydrology (dry and wet seasons) of the Doce River basin and regional ocean circulation. During January and February, corresponding to the main reproductive period of *U. cordatus*, the BC is baroclinically intensified and centered near the 200–300 m isobath, with mean surface velocities between 0.5 and 1.0 m s^{-1} [30,33]. Under these conditions, advection dominates the surface flow, promoting southward transport from all estuarine sources (Figure 3). Larvae released from the Doce River and Piraquê-Açu-Mirim were predominantly advected southward along the continental slope, as indicated by elongated dispersal trajectories, larger median dispersal distances, and the downstream concentration of final larval positions (Figures 2a, 2b, and 6). In contrast, larvae released from Caravelas and São Mateus exhibited shorter trajectories, higher local retention, and recurrent clustering over the Abrolhos Bank (Figures 2a, 6, and 8), consistent with partial trapping within this region. These contrasting dispersal patterns reflect the marked morphological asymmetry of the shelf, where the narrow southern sector favours export-dominated transport, while the wider Abrolhos Bank, with its complex topography and reef structures, promotes local recirculation and longer larval residence times [35].

The mesoscale circulation structures underlying these dispersal contrasts are further evidenced by the relative vorticity fields (Figure 8). During January–April, the vorticity maps show a persistent band of negative vorticity extending from approximately 19.0°S to 20.7°S, south of the Doce River mouth, delineating the same latitudinal corridor along which larvae released from Doce River and Piraquê-Açu-Mirim are transported downstream in the simulations (Figure 2a). Embedded within this band, a semi-stationary cyclonic–anticyclonic pair offshore of 19.5–20.0°S corresponds to the curvature observed in several trajectories as particles veer offshore before re-entering the shelf. Farther north, near São Mateus (18.5–19.0°S), alternating dipole structures in the vorticity fields align with the bifurcation of simulated trajectories during certain months, whereas the Caravelas sector (17.5–18.5°S) exhibits weaker and more fragmented vorticity features, consistent with the more spatially confined dispersal patterns observed for this spawning region.

© 2026 by the author(s). Distributed under a Creative Commons CC BY license.

Preprints.org (www.preprints.org) | NOT PEER-REVIEWED | Posted: 24 March 2026 doi:10.20944/preprints202603.1937.v1

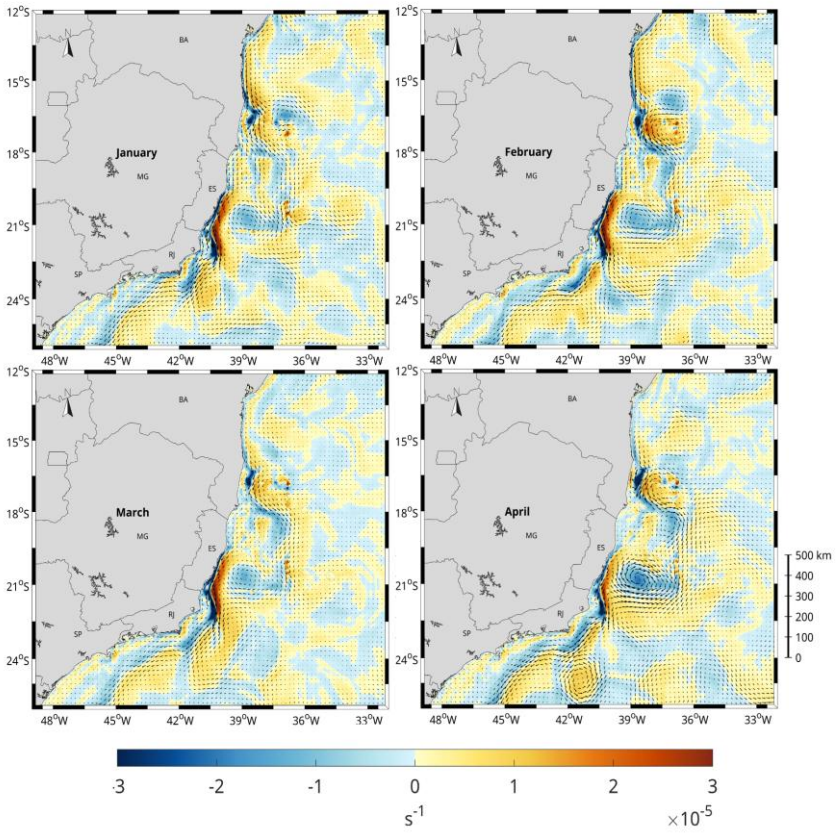

Figure 8. Mean relative vorticity fields (January–April) over the southeastern Brazilian shelf. Negative values (blue tones) indicate regions of enhanced horizontal shear and surface-layer divergence, while positive values (red tones) represent convergent circulation. Arrows show surface current vectors derived from the model. The persistent negative-vorticity band south of the Doce River mouth (19–20.7°S) and the dipole structure near São Mateus (18.5–19°S) correspond to the main dispersal corridors followed by simulated *U. cordatus* larvae.

As the season advances into March and April, circulation reorganizes in response to intensified north-easterly winds that induce upwelling of South Atlantic Central Water (SACW) between Prado and Vitória [58,59]. The resulting vertical shear and isopycnal tilting enhance mesoscale activity of the Abrolhos anticyclonic eddy near 18–19°S, which favors convergence and retention, and the Vitória cyclonic eddy around 21–22°S, which drives divergence and offshore export [33,60]. The simulated final larval distributions (Figure 5) reflect the contrasting dispersal regimes identified in the connectivity and retention analyses. North of 20°S, particle accumulation over the Abrolhos Bank coincides with higher local retention and repeated connections among northern spawning sites, as shown by the connectivity matrices and retention patterns (Figure 8). In contrast, larvae released south of the bank show limited local retention and predominantly downstream connections, consistent with the southward transport pathways observed in the trajectory analyses and resulting in continuous export along the Espírito Santo shelf (Figures 6 and 8). Hydrographic surveys in the same region have documented these quasi-stationary eddies and their influence on particle retention and nutrient recirculation [58], supporting the circulation structure revealed in this study.

Thermal and vertical structures associated with upwelling events had a strong effect on survival. SACW intrusions reduced surface temperatures to 17–20 °C [58], close to the lower thermal tolerance limits observed for *U. cordatus* larvae [19,48]. The coincidence between cold intrusions and low survival in the simulations (Figure 4b) suggests that temperature and turbulence act jointly as mortality drivers. Enhanced vertical shear during upwelling likely displaced early stages offshore, reducing their retention near estuarine fronts. Similar patterns of temperature-induced mortality have been reported for tropical decapod and fish larvae under comparable hydrographic conditions

© 2026 by the author(s). Distributed under a Creative Commons CC BY license.

Preprints.org (www.preprints.org) | NOT PEER-REVIEWED | Posted: 24 March 2026 doi:10.20944/preprints202603.1937.v1

[61,62]. This sequence defines a restricted temporal window for larval development and recruitment under seasonal alternation between stratified and upwelling-dominated regimes. The interannual contrast between strongly stratified, curl-active years (2022–2023) and the vertically homogeneous structure observed in 2024 therefore provides a physical explanation for the distinct mortality patterns detected across regions.

Larval dispersal along the eastern Brazilian coast emerges from the coupled action of mesoscale circulation, environmentally driven mortality, and exposure to plume-influenced waters, as jointly expressed by the survival patterns, final larval distributions, and connectivity matrices (Figures 3, 5, and 8). Simulated trajectories show substantial overlap with regions of elevated msPAF associated with the Doce River plume, indicating recurrent exposure to metal-enriched waters dominated by Fe, Cu, Zn, and Al (Figure 5), consistent with post-disaster contamination patterns [27,63]. This exposure differs systematically among regions: larvae released from Caravelas and São Mateus experience longer residence within plume-affected waters (6–15 days) under semi-retentive conditions promoted by recirculation over the Abrolhos Bank, whereas larvae originating from the Doce River and Piraquê-Açu-Mirim experience shorter exposure periods (2–6 days) but are more frequently exported downstream under intensified Brazil Current transport (Figures 5 and 8). Periods of enhanced vertical thermal gradients and shear associated with SACW intrusions coincide with increased temperature-driven mortality (Figure 3), superimposing physiological stress on larvae that are simultaneously advected or retained within contaminated waters. As upwelling-favorable conditions develop, circulation over the Abrolhos Bank shifts toward increased local retention, reinforcing repeated connections among northern estuaries, while south of the bank the Vitória Eddy sustains offshore and downstream export, limiting retention and strengthening asymmetric connectivity (Figures 5 and 8). Together, these coupled physical, chemical, and biological processes generate a persistent spatial asymmetry in connectivity, in which northern estuaries (Caravelas and São Mateus) operate as semi-retentive systems with prolonged exposure to moderate contamination, whereas southern estuaries (Doce River and Piraquê Açu-Mirim) function as export-dominated pathways more frequently subjected to intense contaminant advection and environmentally driven losses. In this context, the negative-vorticity corridor identified south of the Doce River mouth (Figure 7) overlaps spatially with regions of elevated msPAF values (Figure 5), indicating that larvae repeatedly traverse zones of enhanced chemical exposure along their dispersal pathways, rather than encountering contamination only at their final destinations.

Superimposed on this spatially asymmetric connectivity regime, interannual variability further modulated both the magnitude and direction of larval transport. In 2023, El Niño–like conditions deepened the thermocline and weakened wind stress, strengthening the Brazil Current and promoting offshore advection, which extended dispersal distances and reduced local retention [64,65]. In contrast, during 2024 the Brazil Current weakened and shelf recirculation intensified, resulting in shorter trajectories and stronger confinement over the shelf (Figure 3b). These alternating dispersal regimes are consistent with previous assessments of the sensitivity of the Brazil Current to large-scale atmospheric forcing [32,33,58]. Consistent with these transport shifts, the thermal structure of the upper ocean also varied substantially among years, with stronger Brazil Current conditions associated with larger vertical temperature gradients and prolonged stratification, whereas 2024 exhibited weaker gradients. This coupled variability in transport and stratification provides the physical context for the contrasting mortality and retention patterns observed among years.

5. Conclusions

Coastal connectivity of the mud crab *U. cordatus* along the eastern Brazilian coast is driven by mesoscale circulation, vertical thermal structure. We show that larval exposure to plume-influenced waters associated with the Fundão dam collapse is intimately associated with this connectivity. The integration of Lagrangian simulations with in-situ contaminant monitoring and spatially explicit

© 2026 by the author(s). Distributed under a Creative Commons CC BY license.

Preprints.org (www.preprints.org) | NOT PEER-REVIEWED | Posted: 24 March 2026 doi:10.20944/preprints202603.1937.v1

exposure metrics demonstrate that transport pathways regulate not only connectivity among estuaries but also the duration and intensity of larval exposure to environmental stressors.

Connectivity patterns are spatially asymmetric across the region. Northern estuaries associated with the Abrolhos Bank function as semi-retentive systems, where enhanced recirculation promotes local retention and repeated exchange but also prolongs residence within contaminated waters. In contrast, southern estuaries operate as export-dominated pathways, where intensified along-shelf transport favours downstream dispersal, shorter residence times, and more frequent advective losses.

Interannual variability further modulates these outcomes. Stronger Brazil Current conditions enhance dispersal distances, stratification, and thermal stress, whereas weaker circulation and intensified shelf recirculation promote confinement and alter the balance between retention, exposure, and mortality. Although direct toxic mortality was not quantified, the recurrent overlap between larval trajectories and metal-enriched waters identifies persistent pathways of potential sublethal stress that may influence recruitment across connected mangrove systems. Future work should consider monitoring of *U. cordatus* in affected areas, to evaluate possible impacts in population structure. The present research represents a marine connectivity oriented contribution to a beyond borders disaster evaluation approach and may orient future investigations.

Supplementary Materials: The following supporting information can be downloaded at the website of this paper posted on Preprints.org, Figure S1. Validation of the daily time series between the model and the moorings for sea level, cross-shelf velocity, and along-track velocity; Table S1. Spearman's correlation (R) and Root Mean Square Error (RMSE) of between in situ and mooring points of oceanografic variables; Figure S2. Climatology of wind direction and intensity for the months of January, February, March, and April in the years 2022, 2023, and 2024; Table S2. Wind direction occurrences (%) from January to April in 2022, 2023, and 2024 for the region encompassing PMBA/Fest mooring 3, located at 39.73°W and 19.60°S; Table S3. Wind direction occurrences (%) from January to April 2022 for the region encompassing PMBA/Fest mooring 3, located at 39.73°W and 19.60°S; Table S4. Wind direction occurrences (%) from January to April 2023 for the region encompassing PMBA/Fest mooring 3, located at 39.73°W and 19.60°S; Table S5. Wind direction occurrences (%) from January to April 2024 for the region encompassing PMBA/Fest mooring 3, located at 39.73°W and 19.60°S; Figure S6. Climatology of current direction per year (Caravelas, São mateus, Doce River and Piraquê açu-Mirim); Figure S7. Climatology of current direction per month to caravelas between january to april of 2022, 2023 and 2024; Figure S8. Climatology of current direction per month to São mateus between january to april of 2022, 2023 and 2024; Figure S9. Climatology of current direction per month to Doce River between january to april of 2022, 2023 and 2024; Figure S10. Climatology of current direction per month to Piraquê açu-Mirim between january to april of 2022, 2023 and 2024.

Author Contributions: Conceptualization, N.G., M.D., K.O., N.S., M.T and B.F.; methodology, N.G., S.F., L. M., M.S., M.T and B.F.; software, N.G., S.F., L.M and D.G.; validation, N.G., S.F., L.M and M.S.; formal analysis, N.G., S.F., L.M and M.S.; investigation, N.G., S.F, L.M., M.S., D.G., G.P., M.T., I.S and B.F.; data curation, N,G., S.F., L.M., M.S and B.F.; writing—original draft preparation, N.G., S.F., L.M and B.F.; All authors writing—review and editing.

Data Availability Statement: Data will be made available on request

Acknowledgments: The present study was developed with turbidity data of the Aquatic Biodiversity Monitoring ProgramPMBA, established by the Technical-Scientific Agreement (001/2018) between UFES-FEST-Renova Foundation.

Conflicts of Interest: The authors declare no conflicts of interest.

© 2026 by the author(s). Distributed under a Creative Commons CC BY license.

Preprints.org (www.preprints.org) | NOT PEER-REVIEWED | Posted: 24 March 2026 doi:10.20944/preprints202603.1937.v1

References

1. Marta-Almeida, M.; Mendes, R.; Amorim, F.N.; Cirano, M.; Dias, J.M. Fundão dam collapse: Oceanic dispersion of River Doce after the greatest Brazilian environmental accident. Mar. Pollut. Bull. **2016**, 112, 359–364. https://doi.org/10.1016/j.marpolbul.2016.07.039.
2. Francini-Filho, R.B.; et al. Remote sensing, isotopic composition and metagenomics analyses revealed Doce River ore plume reached the southern Abrolhos Bank Reefs. Sci. Total Environ. **2019**, 697, 134038. https://doi.org/10.1016/j.scitotenv.2019.134038.
3. Rudorff, N.; Rudorff, C.M.; Kampel, M.; Ortiz, G. Remote sensing monitoring of the impact of a major mining wastewater disaster on the turbidity of the Doce River plume off the eastern Brazilian coast. ISPRS J. Photogramm. Remote Sens. **2018**, 145, 349–361. https://doi.org/10.1016/j.isprsjprs.2018.02.013.
4. Magris, R.A.; Marta-Almeida, M.; Monteiro, J.A.F.; Ban, N.C. A modelling approach to assess the impact of land mining on marine biodiversity: Assessment in coastal catchments experiencing catastrophic events (SW Brazil). Sci. Total Environ. **2019**, 659, 828–840. https://doi.org/10.1016/j.scitotenv.2018.12.238.
5. Tognella, M.M.P.; Falqueto, A.R.; Espinoza, H.D.C.F.; Gontijo, I.; Gontijo, A.B.P.L.; Fernandes, A.A.; Schmildt, E.R.; Soares, M.L.G.; Chaves, F.O.; Schmidt, A.J.; Lopes, D.M.S.; Barcelos, U.D.; d'Addazio, V.; Lima, K.O.O.; Pascoalini, S.S.; Paris, J.O.; Brites Júnior, N.V.; Porto, L.A.; Almeida Filho, E.; Oliveira, C.P.; Leopoldo, R.V.S.; Leite, S.; Berribilli, M.P.; Vieiras, S.F.R.; Rosa, M.B.; Sá, F.; Neto, R.R.; Ghisolfi, R.D.; Castro, M.S.M.; Rigo, D.; Tosta, V.C.; Albino, J. Mangroves as traps for environmental damage to metals: The case study of the Fundão Dam. Sci. Total Environ. **2022**, 806, 150452. https://doi.org/10.1016/j.scitotenv.2021.150452.
6. Neves, A.C.O.; Nunes, F.P.; Carvalho, F.A.; Fernandes, G.W. Neglect of ecosystem services by mining and the worst environmental disaster in Brazil. Perspect. Ecol. Conserv. **2016**, 14, 24–27. https://doi.org/10.1016/j.ncon.2016.03.002.
7. Carmo, F.F.; Kamino, L.H.Y.; Junior, R.T.; Campos, I.C.; Silvino, G.; Pinto, C.E.F. Fundão tailings dam failures: The environmental tragedy of the largest technological disaster of Brazilian mining in a global context. Perspect. Ecol. Conserv. **2017**, 15, 145–151. https://doi.org/10.1016/j.pecon.2017.06.002.
8. Franks, D.M.; Stringer, M.; Torres-Cruz, L.A.; Baker, E.; Valenta, R.; Thygesen, K.; et al. Tailings facility disclosures reveal stability risks. *Sci. Rep.* 2021, *11*, 5353. doi: 10.1038/s41598-021-84897-0.
9. IBAMA. Preliminary technical report: Environmental impacts resulting from the disaster involving the collapse of the Fundão dam in Mariana, Minas Gerais; Brazilian Institute of Environment and Renewable Natural Resources: Brasília, Brazil, 2015.
10. Oliveira, K.S.S.; Quaresma, V.S. Temporal variability in the suspended sediment load and streamflow of the Doce River. J. S. Am. Earth Sci. **2017**, 78, 101–115. https://doi.org/10.1016/j.jsames.2017.06.009.
11. Lopes, S.M.D.; Chaves, O.F.; Tognella, M.M.P. Mangrove mortality: Analyses of natural and anthropic causes and their effects on forest dynamics. J. Coast. Res. **2020**, 95, 102–107. doi: 10.2112/SI95-020.1.
12. Lima, K.O.O.; Tognella, M.M.P.; Schmidt, A.J.; Schmildt, E.R.; Porto, L.A.; Almeida Filho, E.; Gontijo, I. Baseline study of *Ucides cordatus* populations and the contribution to the management of these social and economic resources. Wetlands **2023**, 43, 28. https://link.springer.com/article/10.1007/s13157-023-01676-5.
13. Pascoalini, S.S.; et al. Iron and manganese concentrations in leaf tissues of Rhizophora mangle (Rhizophoraceae): Implications for energetic metabolism. Rev. Biol. Trop. **2024**, 72, e56835. doi: 10.15517/rev.biol.trop..v72i1.56835.
14. Diele, K.; Koch, V.; Saint-Paul, U. Population structure, catch composition and CPUE of the artisanally harvested mangrove crab Ucides cordatus (Ocypodidae) in the Caeté estuary, North Brazil: Indications for overfishing? Aquat. Living Resour. **2005**, 18, 169–178. https://doi.org/10.1051/alr:2005018.
15. Oliveira-Neto, J.F.; Pie, M.R.; Boeger, W.A.; Ostrensky, A.; Baggio, R.A. Population genetics and evolutionary demography of Ucides cordatus (Decapoda: Ocypodidae). Mar. Ecol. **2007**, 28, 460–469. doi: 10.1111/j.1439-0485.2007.00188.x.
16. Firmo, A.; Tognella, M.; Silva, S.; Barboza, R.; Alves, R. Capture and commercialization of blue land crabs ("guaiamum") Cardisoma guanhumi (Latreille, 1825) along the coast of Bahia State, Brazil: An ethnoecological approach. J. Ethnobiol. Ethnomed. **2012**, 8, 12. doi: 10.1186/1746-4269-8-12.

© 2026 by the author(s). Distributed under a Creative Commons CC BY license.

Preprints.org (www.preprints.org) | NOT PEER-REVIEWED | Posted: 24 March 2026 doi:10.20944/preprints202603.1937.v1

17. Nascimento, D.M.; et al. Commercial relationships between intermediaries and harvesters of the mangrove crab Ucides cordatus (Linnaeus, 1763) in the Mamanguape River Estuary, Brazil, and their socio-ecological implications. Ecol. Econ. **2017**, 131, 44–51. https://doi.org/10.1016/j.ecolecon.2016.08.017.
18. Bromenschenkel, V.C.S.; Tognella, M.M.P. Population estimate and extractive potential of uçá crab in the post-closed season: Subsidies for management in a conservation unit of sustainable use. Res. Soc. Dev. **2020**, 9. https://doi.org/10.33448/rsd-v9i12.10992.
19. Rodrigues, M.D.; Hebling, N.J. Ucides cordatus cordatus (Linnaeus, 1763) (Crustacea, Decapoda): Complete larval development under laboratory conditions and its systematic position. Rev. Bras. Zool. **1989**, 6, 147–166. https://doi.org/10.1590/S0101-81751989000100016.
20. Abrunhosa, F.; Melo, M.; Abrunhosa, J. Development and functional morphology of the foregut of larvae and postlarvae of Ucides cordatus (Decapoda, Ocypodidae). Nauplius **2003**, 11, 37–43.
21. Diele, K.; Simith, D.J.B. Salinity tolerance of northern Brazilian mangrove crab larvae, Ucides cordatus (Ocypodidae): Necessity for larval export? Estuar. Coast. Shelf Sci. **2006**, 68, 600–608. https://doi.org/10.1016/j.jembe.2007.04.008.
22. Diele, K.; Simith, D.J.B. Effects of substrata and conspecific odour on the metamorphosis of mangrove crab megalopae, Ucides cordatus (Ocypodidae). J. Exp. Mar. Biol. Ecol. **2007**, 348, 174–182. https://doi.org/10.1016/j.jembe.2007.04.008.
23. Schmidt, A.J.; Diele, K. First field record of mangrove crab Ucides cordatus (Crustacea: Decapoda: Ucididae) recruits co-inhabiting burrows of conspecific crabs. Zoologia (Curitiba) 2009, 26, 792–794. doi: 10.1590/S1984-46702009000400026.
24. Melo, G.A.S. *Identification manual of Brachyura (crabs and swimming crabs) from the Brazilian coast*; Editora Plêiade: São Paulo, Brazil, 1996.
25. Britto, F.; et al. Population connectivity and larval dispersal of the exploited mangrove crab Ucides cordatus along the Brazilian coast. PeerJ **2018**, 6, e4702. doi: 10.7717/peerj.4702.
26. Ventura-Lima, J.; Bogo, M.R.; Monserrat, J.M. Accumulation, biotransformation, and biochemical responses after exposure to arsenite and arsenate in the estuarine polychaete *Laeonereis acuta* (Nereididae). *Environ. Sci. Pollut. Res.* 2011, *18*, 1270–1278. doi: 10.1007/s11356-011-0478-4.
27. Fernandes, L.F.L.; Paiva, T.R.M.; Longhini, C.M.; Pereira, J.B.; Ghisolfi, R.D.; Lázaro, G.C.S.; Rocha, G.M. Marine zooplankton dynamics after a major mining dam rupture in the Doce River, southeastern Brazil: Rapid response to a changing environment. *Sci. Total Environ.* 2020, *736*, 139621. doi: 10.1016/j.scitotenv.2020.139621.
28. Mortimer, M.R.; Miller, G.J. Susceptibility of larval and juvenile instars of the sand crab, *Portunus pelagicus* (L.), to seawater contaminated by chromium, nickel or copper. *Aust. J. Mar. Freshw. Res.* 1994, *45*, 1107–1121. https://doi.org/10.1071/MF9941107.
29. Anger, K. *The Biology of Decapod Crustacean Larvae*; A.A. Balkema Publishers: Lisse, The Netherlands, 2001.
30. Rodrigues, R.R.; Rothstein, L.M.; Wimbush, M. Seasonal variability of the South Equatorial Current bifurcation in the Atlantic Ocean: A numerical study. *J. Phys. Oceanogr.* 2007, *37*, 16–30. doi: 10.1175/JPO2983.1.
31. Luko, C.D.; da Silveira, I.C.A.; Simoes-Sousa, I.T.; Araujo, J.M.; Tandon, A. Revisiting the Atlantic South Equatorial Current. *J. Geophys. Res. Ocean.* 2021, *126*, e2021JC017387. https://doi.org/10.1029/2021JC017387.
32. Soutelino, R.G.; Gangopadhyay, A.; da Silveira, I.C.A. The roles of vertical shear and topography on the eddy formation near the site of origin of the Brazil Current. *Cont. Shelf Res.* 2013, *70*, 46–60. https://doi.org/10.1016/j.csr.2013.10.001.
33. Arruda, W.Z.; da Silveira, I.C.A. Dipole-induced Central Water extrusions south of Abrolhos Bank (Brazil, 20.5°S). *Cont. Shelf Res.* 2019, *188*, 103976. https://doi.org/10.1016/j.csr.2019.103976.
34. Silveira, I.C.A.; Calado, L.; Castro, B.M.; Cirano, M.; Lima, J.A.M.; Mascarenhas, A.D.S. On the baroclinic structure of the Brazil Current–Intermediate Western Boundary Current system at 22–23°S. *Geophys. Res. Lett.* 2004, *31*, L14308. doi: 10.1029/2004GL020036.
35. Bastos, A.C.; Quaresma, V.S.; Marangoni, M.B.; D'Agostini, D.P.; Bourguignon, S.N.; Cetto, P.H.; Collins, M. Shelf morphology as an indicator of sedimentary regimes: A synthesis from a mixed siliciclastic–

© 2026 by the author(s). Distributed under a Creative Commons CC BY license.

Preprints.org (www.preprints.org) | NOT PEER-REVIEWED | Posted: 24 March 2026 doi:10.20944/preprints202603.1937.v1

carbonate shelf on the eastern Brazilian margin. *J. S. Am. Earth Sci.* 2015, *63*, 125–136. doi:10.1016/j.jsames.2015.07.003.

36. Auclair, F.; Benshila, R.; Bordois, L.; Boutet, M.; Brémond, M.; Caillaud, M.; Cambon, G.; Capet, X.; Debreu, L.; Ducousso, N.; Dufois, F.; Dumas, F.; Ethé, C.; Gula, J.; Hourdin, C.; Illig, S.; Jullien, S.; Le Corre, M.; Le Gac, S.; et al. Coastal and regional ocean community model (1.2.1); Zenodo: Geneva, Switzerland, 2022.
37. Jullien, S.; Caillaud, M.; Benshila, R.; Bordois, L.; Cambon, G.; Dumas, F.; Le Gentil, S.; Lemarié, F.; Marchesiello, P.; Theetten, S.; Dufois, F.; Le Corre, M.; Morvan, G.; Le Gac, S.; Gula, J.; Pianezze, J.; Schreiber, M.; Schaefer, A.-L.; Valat, S. CROCO technical and numerical documentation (2.1.0); Zenodo: Geneva, Switzerland, 2025.
38. Shchepetkin, A.F.; McWilliams, J.C. The regional oceanic modeling system (ROMS): A split-explicit, free-surface, topography-following-coordinate oceanic model. *Ocean Model.* 2005, *9*, 347–404. doi: 10.1016/j.ocemod.2004.08.002.
39. Debreu, L.; Marchesiello, P.; Penven, P.; Cambon, G. Two-way nesting in split-explicit ocean models: Algorithms, implementation and validation. *Ocean Model.* 2012, *49–50*, 1–21. https://doi.org/10.1016/j.ocemod.2012.03.003.
40. GEBCO Bathymetric Compilation Group. The GEBCO_2024 grid: A continuous terrain model of the global oceans and land. 2024. doi: 10.5285/1c44ce99-0a0d-5f4f-e063-7086abc0ea0f.
41. Hersbach, H.; et al. ERA5 hourly data on single levels from 1940 to present; Copernicus Climate Change Service (C3S) Climate Data Store (CDS): Reading, UK, 2023.
42. Egbert, G.; Erofeeva, S. Efficient inverse modeling of barotropic ocean tides. *J. Atmos. Ocean. Technol.* 2002, *19*, 183–204. doi: 10.1175/1520-0426(2002)019%3c0183:EIMOBO%3e2.0.CO;2.
43. HYCOM. Hybrid Coordinate Ocean Model; Consortium for Data Assimilative Modeling: 2015.
44. Lett, C.; et al. A Lagrangian tool for modelling ichthyoplankton dynamics. *Environ. Model. Softw.* 2008, *23*, 1210–1214. https://doi.org/10.1016/j.envsoft.2008.02.005.
45. Diele, K. Life history and population structure of the exploited mangrove crab *Ucides cordatus cordatus* (Decapoda: Brachyura) in the Caeté estuary, North Brazil. *Ph.D. Thesis*, University of Bremen, Bremen, Germany, 2000.
46. Goes, P.; et al. Bioecology of uçá crab, *Ucides cordatus* (Linnaeus, 1763), in Vitória Bay, Espírito Santo, Brazil. *Braz. J. Oceanogr.* 2010, *58*, 153–163. https://doi.org/10.1590/S1679-87592010000200006.
47. Silva, U.T. Population recovery of the mangrove crab *Ucides cordatus* (Linnaeus, 1763) through the release of immature stages in anthropogenically impacted areas. *Ph.D. Thesis*, Universidade Federal do Paraná, Curitiba, Brazil, 2007.
48. Cottens, K.F.; Silva, U.A.; Becker, A.G.; Iosafat, P. Variation in survival rate and development time of *Ucides cordatus* (Linnaeus, 1763) larvae cultured under different temperatures. *Bol. Téc. Cient. CEPNOR* 2010, *10*, 67–78. https://d1wqtxts1xzle7.cloudfront.net/34560090/Artigo_5-2010-libre.pdf?1409223155=&response-content-disposition=inline%3B+filename%3DA_VARIACAO_DA_TAXA_DE_SOBREVIVENCIA_E_DO.pdf&Expires=1773943498&Signature=Mv2RvqlogXlDzqn-BKF6CxO5-bXVP9Wbq3KZOgkApOeT1VEkwbL22UIomHAEhYjUUyJofQAAXr5rl-st4zNXnQIKaYBbn4w8fVsQcjMYfR-fNFIIvnIMRJ92SRwtWs9HVQKovp0CiXytbX1U759aVMszLd2fxSjMOzZjPsrh4NCEyM~mue8cu0gOLIok9d7pc6Ecb7lezEew6Byf2~QX7SPwZcaBgAWC0YDR8adbNLWyZ2BUflyhMMRXo8DD6POsMFycepBTenlFkNTvXxeTu1sUQLlHjSRltGLOWBzsVWspI87srC7u92x3qn3Hwcof0-UjroV22LbnOwjGrr5utg__&Key-Pair-Id=APKAJLOHF5GGSLRBV4ZA.
49. Peliz, A.; Marchesiello, P.; Dubert, J.; Marta-Almeida, M.; Roy, C.; Queiroga, H. A study of crab larvae dispersal on the Western Iberian Shelf: Physical processes. *J. Mar. Syst.* 2007, *68*, 215–236. https://doi.org/10.1016/j.jmarsys.2006.11.007.
50. Longhini, C.M.; Rodrigues, S.K.; Costa, E.S.; Silva, C.A.; Cagnin, R.C.; Gripp, M.; Sá, F. Environmental quality assessment in a marine coastal area impacted by mining tailings using a geochemical multi-index and physical approach. *Sci. Total Environ.* 2022, *803*, 149883. doi: 10.1016/j.scitotenv.2021.149883.

© 2026 by the author(s). Distributed under a Creative Commons CC BY license.

Preprints.org (www.preprints.org) | NOT PEER-REVIEWED | Posted: 24 March 2026 doi:10.20944/preprints202603.1937.v1

51. Posthuma, L.; van Gils, J.; Zijp, M.C.; van de Meent, D.I.K.; de Zwart, D. Species sensitivity distributions for use in environmental protection, assessment, and management of aquatic ecosystems for 12,386 chemicals. *Environ. Toxicol. Chem.* 2019, *38*, 905–917. doi:10.1002/etc.4373.
52. Alvares, C.A.; Stape, J.L.; Sentelhas, P.C.; Gonçalves, J.L.M.; Sparovek, G. Köppen's climate classification map for Brazil. *Meteorol. Z.* 2013, *22*, 711–728. doi:10.1127/0941-2948/2013/0507.
53. Bunting, P.J.; et al. The Global Mangrove Watch—A new 2010 baseline of mangrove extent. *Remote Sens.* 2018, *10*, 1669. doi: 10.3390/rs10101669.
54. Castelao, R.M.; Barth, J.A. Upwelling around Cabo Frio, Brazil: The importance of wind stress curl. *Geophys. Res. Lett.* 2006. https://doi.org/10.1029/2005GL025182.
55. Bravo, L.; Ramos, M.; Astudillo, O.; Dewitte, B.; Goubanova, K. Seasonal variability of the Ekman transport and pumping in the upwelling system off central-northern Chile (~30°S). *Ocean Sci.* 2016, *12*, 1049–1065. doi: 10.5194/os-12-1049-2016.
56. Song, H.; Marshall, J.; McGillicuddy, D.J.; Seo, H. Impact of current–wind interaction on vertical processes in the Southern Ocean. *J. Geophys. Res. Ocean.* 2020, *125*, e2020JC016046. https://doi.org/10.1029/2020JC016046.
57. Ghisolfi, R.D.; et al. Physical forcing mechanisms controlling the variability of chlorophyll-a over the Royal-Charlotte and Abrolhos Banks—Eastern Brazilian Shelf. *PLoS ONE* 2015, *10*, e0117082. doi: 10.1371/journal.pone.011708.
58. Campos, E.J.D.; Velhote, D.; da Silveira, I.C.A. Shelf break upwelling driven by Brazil Current cyclonic meanders. *Geophys. Res. Lett.* 2000, *27*, 751–754. https://doi.org/10.1029/1999GL010502.
59. Castro-Filho, B.M.; Lorenzzetti, J.A.; Silveira, I.C.A.; Miranda, L.B.; Rossi-Wongtschowski, C.L.D.B. Thermohaline structure and circulation in the region between Cabo de São Tomé (RJ) and Chuí (RS). In *The Oceanographic Environment of the Continental Shelf and Slope in the Southeast–South Region of Brazil*; Rossi-Wongtschowski, C.L.D.B., Madureira, L.S.P., Eds.; EDUSP: São Paulo, Brazil, 2006.
60. Mazzini, P.L.F.; Barth, J.A. A comparison of mechanisms generating vertical transport in the Brazilian coastal upwelling regions. *J. Geophys. Res. Ocean.* 2013, *118*, 5977–5993. doi:10.1002/2013JC008924.
61. Bonecker, S.L.C.; Araujo, A.V.; Carvalho, P.F.; Dias, C.O.; Fernandes, L.F.; Migotto, A.E.; Oliveira, O.M.P. Horizontal and vertical distribution of mesozooplankton species richness and composition down to 2300 m in the Southwest Atlantic Ocean. *Zoologia (Curitiba)* 2014, *31*, 445–462. doi:10.1590/S1984-46702014000500005.
62. Franco, B.C.; Defeo, O.; Piola, A.R.; Barreiro, M.; Yang, H.; Ortega, L.; Möller, O.O. Climate change impacts on the atmospheric circulation, ocean, and fisheries in the southwest South Atlantic Ocean: A review. *Clim. Change* 2020, *162*, 2359–2377. doi: 10.1007/s10584-020-02783-6.
63. Hatje, V.; Masqué, P.; Patire, V.F.; Dórea, A.; Barros, F. Blue carbon stocks, accumulation rates, and associated spatial variability in Brazilian mangroves. *Limnol. Oceanogr.* 2021, *66*, 321–334. doi:10.1002/lno.11607.
64. Pezzi, L.P.; Souza, R.B.; Santini, M.F.; Miller, A.J.; Carvalho, J.T.; Parise, C.K.; Rubert, J. Oceanic eddy-induced modifications to air–sea heat and CO_2 fluxes in the Brazil–Malvinas Confluence. *Sci. Rep.* 2021, *11*, 10648. doi:10.1038/s41598-021-89985-9.
65. Araujo, G.S.; Rocha, L.A.; Lastrucci, N.S.; Luiz, O.J.; Di Dario, F.; Floeter, S.R. The Amazon–Orinoco barrier as a driver of reef-fish speciation in the Western Atlantic through time. *J. Biogeogr.* 2022, *49*, 1407–1419. doi: 10.1111/jbi.14398.

Disclaimer/Publisher's Note: The statements, opinions and data contained in all publications are solely those of the individual author(s) and contributor(s) and not of MDPI and/or the editor(s). MDPI and/or the editor(s) disclaim responsibility for any injury to people or property resulting from any ideas, methods, instructions or products referred to in the content.

© 2026 by the author(s). Distributed under a Creative Commons CC BY license.